Dissipative transport of a Bose-Einstein condensate

D. Dries, S. E. Pollack, J. M. Hitchcock, and R. G. Hulet

Department of Physics and Astronomy and Rice Quantum Institute, Rice University, Houston, Texas 77005, USA

We investigate the effects of impurities, either correlated disorder or a single Gaussian defect, on the collective dipole motion of a Bose-Einstein condensate of ^{7}Li in an optical trap. We find that this motion is damped at a rate dependent on the impurity strength, condensate center-of-mass velocity, and interatomic interactions. Damping in the Thomas-Fermi regime depends universally on the disordered potential strength scaled to the condensate chemical potential and the condensate velocity scaled to the speed of sound. The damping rate is comparatively small in the weakly interacting regime, and, in this case, is accompanied by strong condensate fragmentation. *In situ* and time-of-flight images of the atomic cloud provide evidence that this fragmentation is driven by dark soliton formation.

I. INTRODUCTION

The creation of Bose-Einstein condensates (BECs) of ultracold atomic gases [1–3] has enabled investigations of some of the most fundamental concepts of condensed matter physics [4]. One of the most fruitful avenues of research has involved the use of BECs to probe the nature of superfluidity itself. Early studies led to observations of the critical velocity for the onset of dissipation [5–7] and quantized vortices [8–11].

Recently, there has been much interest in using BECs to emulate disordered superfluids (cf. Refs. [12,13]). Results from such experiments have wide ranging implications, from the transport of superfluid He in porous media [14] to the motion of atomic BECs in microchip traps or matter waveguides [15–18]. Of particular interest is how disorder can disrupt, or can even destroy, superfluidity. Due to their exquisite controllability, atomic BECs are ideal physical systems with which to systematically study the interplay between superfluidity, disorder, and interatomic interactions.

In this paper, we report measurements of the dissipation of the superfluid flow of an elongated BEC subject to either a disordered potential or a single Gaussian defect. We characterize the superfluid nature of the harmonically trapped cloud through detailed measurements of the velocity-dependent damping of the collective dipole mode. We use a BEC of ^{7}Li in the $|F = 1, m_F = 1\rangle$ internal state, where the interactions may be tuned via a wide Feshbach resonance located at 737 G [19–21]. This resonance includes a shallow zero-crossing that enables the s-wave scattering length a to be tuned over a range of nearly seven decades, with a as small as $0.01 a_0$, where a_0 is the Bohr radius [21]. The gas may be made nearly ideal with transport properties strikingly different from the more strongly interacting case. Furthermore, the healing length $\xi = 1/\sqrt{8\pi n_0 a}$, where n_0 is the peak density of the condensate, may be made as large as the condensate itself. In this regime, effects due to the fundamental wave nature of individual atoms become important. For example, if ξ is on the order of the disorder grain size or larger, a BEC can become an Anderson localized insulator [22,23]. In addition, the chemical potential μ in this weakly interacting regime may be less than the radial harmonic oscillator ground-state energy, which effectively freezes out the radial dynamics and leads to quasi-one-dimensional (quasi-1D) behavior.

A. Superfluidity of a BEC

One of the seminal results originating from the theory of superfluid ^{4}He is Landau's criterion. According to this criterion, elementary excitations can be created only if the fluid velocity v is greater than Landau's critical velocity v_L [24,25],

$$v_L = \min \frac{\epsilon(p)}{p}, \tag{1}$$

where $\epsilon(p)$ is the energy of an elementary excitation of momentum p. For the case of a weakly interacting BEC with uniform density n, Bogoliubov theory gives the excitation energy as [26]

$$\epsilon(p) = \sqrt{\left(\frac{p^2}{2m}\right)^2 + c^2 p^2}, \tag{2}$$

where m is the atomic mass and c is the bulk speed of sound. For small p, this spectrum reduces to the well-known relation $\epsilon(p) = cp$, which describes phonon excitations with

$$c = \sqrt{\frac{nU}{m}}, \tag{3}$$

where $U = 4\pi\hbar^2 a/m$. Application of Eq. (1) gives $v_L = c$, which implies that only supersonic flow can dissipate energy through the creation of elementary excitations; conversely, if the flow is subsonic, excitations are energetically forbidden, and the flow is superfluid. Application of Eq. (1) to the case of a noninteracting condensate implies that $v_L = 0$, which suggests that superfluidity cannot exist in an ideal gas.

The dynamics of highly elongated BECs can be accurately modeled by using an effective one-dimensional (1D) nonlinear Schrödinger equation (NLSE) [27–30]. In such a treatment, one starts from the three-dimensional (3D) Gross-Pitaevskii equation (GPE), and integrates out the radial dimension. The effect of this integration is a reduction in c relative to Eq. (3) due to the average over the nonuniform radial density. For the case of a harmonically trapped BEC in the Thomas-Fermi regime, the bulk density n is replaced with the average density $n_0/2$. Therefore, the speed of sound becomes

$$c_0 = \sqrt{\frac{n_0 U}{2m}}. \tag{4}$$

A theoretical description of an elongated BEC beyond the standard 1D NLSE leads to a reduction (on the order of 10%) in the speed of sound relative to Eq. (4) [31]. In addition, the spectrum of axially propagating excitations in a cylindrical BEC can differ dramatically from Eq. (2) when $\mu \gg \hbar\omega_r$, where μ is the chemical potential, which leads to an additional reduction in v_L [32]. The highest μ condensates created in our system have $\mu/\hbar\omega_r \sim 13$, which result in a predicted 20% reduction [32].

When attempting to explain the onset of dissipation in any particular experimental situation, care must be taken to apply Landau's criterion *locally*, by using the local density $n(r = 0, z)$ instead of $n_0 \equiv n(r = 0, z = 0)$ in Eq. (4) [33]. For arbitrary trapping potentials, excitations will be nucleated first in regions of low density where the local speed of sound is small and the critical velocity is reduced relative to the bulk. As a consequence of this effect, experimentally observed critical velocities are often much lower than the bulk speed of sound [5–7].

The remainder of this paper is organized as follows: In Sec. II, we describe our experimental methods for creating a BEC in either a disordered harmonic potential or a harmonic potential with a single Gaussian defect; in Secs. III and IV, we discuss our results for the induced dissipation for these two scenarios, where both the 3D Thomas-Fermi and the quasi-1D weakly interacting regimes are discussed for each case. We conclude in Sec. V with a discussion that relates the similarities and differences between dissipation in the two types of potentials, and directions for future studies.

II. EXPERIMENTAL METHOD

We create a BEC of ^{7}Li in a highly elongated, cylindrically symmetric, hybrid magnetic-optical dipole trap [21,34] with radial and axial trapping frequencies in the ranges of $\omega_r/(2\pi) \sim 220$–460 Hz and $\omega_z/(2\pi) \sim 4$–5.5 Hz, respectively. The radial confinement is dominated by the optical trapping potential formed by a single focused laser beam with a wavelength of 1030 nm and a $1/e^2$ Gaussian radius of 33 μm, while the axial confinement is dominated by an adjustable harmonically confining magnetic field. A set of Helmholtz coils provides a uniform bias field along the z-axis of the trap, which allows for the tuning of a via a Feshbach resonance at 737 G [19–21]. The BEC is created at a field of 717 G where a is positive and large enough ($\sim 200\,a_0$) to allow for efficient evaporative cooling in the optical trap but is small enough to avoid substantial three-body losses. At this field, the trap lifetime is limited to ~ 10 s due to three-body recombination with a loss coefficient of $L_3 \sim 10^{-26}$ cm^6/s [35]. After evaporation, the BEC has no discernible thermal component from which we estimate that the temperature $T < 0.5T_C$, where T_C is the BEC transition temperature. The bias field is then ramped over a time scale on the order of seconds to achieve the desired value for a.

We excite the collective dipole mode of the condensate by pulsing on an axially oriented magnetic gradient, thereby abruptly shifting the center of the harmonic trap. After 1/4 of an oscillation period, the condensate is at the peak of an oscillation, and we abruptly switch on either a disordered potential with an extent exceeding the oscillation amplitude
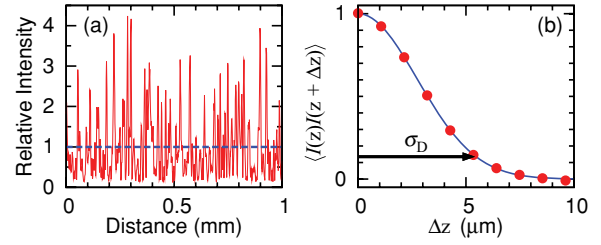

FIG. 1. (Color online) Disordered potential created from laser speckle. (a) Cut through an image of the speckle potential. The disorder strength V_D is proportional to the average value of the intensity $\langle I \rangle$ (dashed line). (b) The autocorrelation of the intensity distribution is well fit by a Gaussian with $1/e^2$ radius $\sigma_D = 5.5$ μm. For some of the data in this paper (Figs. 6, 8, and 10), $\sigma_D = 3.4$ μm.

of the condensate or a single narrow Gaussian defect located near the trap center. By varying the duration of the gradient pulse, we precisely vary the amplitude A of the oscillation, and, therefore, the initial peak velocity v_0 of the condensate center of mass (c.m.), where $v_0 = A\omega_z$. At various times thereafter, we image the cloud to track the c.m. location as well as the shape of the density distribution. We investigate the dependence of the damped dipole motion on v_0, the strength of the disordered potential or single Gaussian defect, and on the value of a.

The disordered potential is an optical speckle pattern created by passing a laser beam through a diffuser plate in a manner similar to previous studies [34,36–38]. This beam is directed perpendicular to the trap z-axis. Figure 1 shows a characteristic intensity slice of the disorder. The disorder speckle size σ_D is defined to be the $1/e^2$ radius of a Gaussian fit to the autocorrelation of the intensity pattern and is measured to be $\sigma_D = 5.5$ μm. The beam has been cylindrically focused such that, in the radial direction, the speckle size is much larger than the radial Thomas-Fermi radius ~ 10 μm, which makes the disorder effectively 1D. We have verified that the intensity distribution of the disorder follows a decaying exponential $P(I) = \langle I \rangle^{-1} e^{-I/\langle I \rangle}$, as expected for fully developed speckle [39]. The average value of the speckle intensity $\langle I \rangle$ determines the disorder strength through the relation $V_D = \hbar\Gamma^2\langle I \rangle/(4I_{sat}\Delta)$, where the transition linewidth $\Gamma = 2\pi \times 5.9$ MHz and the saturation intensity $I_{sat} = 5.1$ mW/cm^2. The detuning from the ^{7}Li $2S \rightarrow 2P$ transition is $\Delta = 2\pi \times 300$ GHz, which produces a repulsive disorder potential. For the strongest disorder used in these studies, off-resonant scattering from the disorder occurs at a rate of ~ 0.1 s^{-1}. The statistical properties of the speckle pattern are measured by direct imaging with a charge-coupled device camera before the optical system is installed onto the experimental apparatus.

A cylindrically focused laser beam is used for the studies that involve a single Gaussian defect. This beam has a Gaussian intensity distribution $I(z,r) = I_0 e^{-2(r^2/w_r^2 + z^2/w_z^2)}$, with beam waists $w_r = 5$ mm and $w_z = 12$ μm. The radial size of the defect w_r is much larger than R_{TF}, which ensures that flow around the defect is suppressed. We conduct experiments by using both a repulsive (blue-detuned) and an attractive (red-detuned) defect with $|\Delta| = 2\pi \times 300$ GHz.
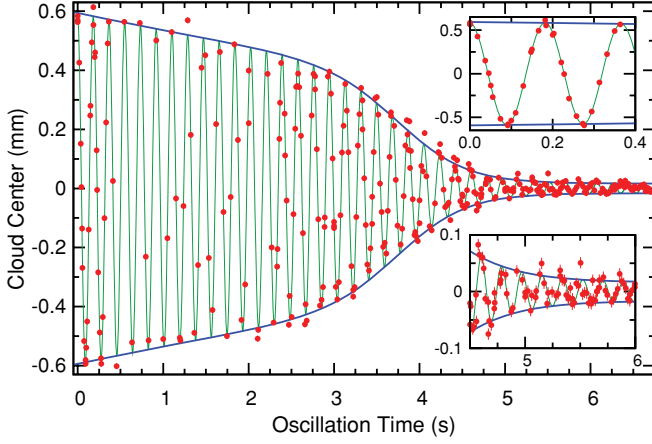
FIG. 2. (Color online) Damping of a condensate initially traveling supersonically through a disordered potential with $V_D/h = 280$ Hz. The center of the BEC (circles) is extracted from a Thomas-Fermi fit to the radially integrated column density (the axial density). The thick lines that trace the amplitude are phenomenological guides to the eye. The initial amplitude is $A = 0.6$ mm, which yields an initial peak velocity of $v_0 = 20$ mm/s. For these data, $\omega_z = 2\pi \times 5.5$ Hz, $\omega_r = 2\pi \times 260$ Hz, $a = 25\,a_0$, and $\mu = \frac{1}{2}m\omega_z^2 R_{\rm TF}^2 = h \times 1.1$ kHz, where $R_{\rm TF}$ is the axial Thomas-Fermi radius. In addition, $c_0 = 5.6$ mm/s, $\xi = 0.8\,\mu$m, and $\xi/\sigma_D = 0.2$. The insets show details of the oscillation at early and late times.

We adjust the healing length through an approximate range $0.5\,\mu$m $< \xi < 20\,\mu$m by tuning a. Thus, a wide range of values is achievable for the relevant dimensionless quantities $0.1 < \xi/\sigma_D < 3.6$ and $0.04 < \xi/w_z < 1.7$.

III. DISORDER-INDUCED DISSIPATION

A. Thomas-Fermi regime

Figure 2 shows the position of the center of a condensate at various times during a dipole oscillation in a disordered potential. The dipole oscillation is initiated by a kick that produces an initial peak velocity of $v_0 = 20$ mm/s when the condensate passes through the center of the trap. For these data, the condensate begins its motion well into the supersonic regime with $v_0 \sim 4c_0$. The resulting oscillation is characterized by a time-dependent damping, which suggests that the damping depends on v_0. The damping rate is initially small, goes through a maximum after about 3.8 s, and then diminishes at later times. We fit four-period sections of the data in Fig. 2 to the form of a damped harmonic oscillator,

$$z(t) = Ae^{-\beta t} \cos(\omega' t + \phi), \qquad (5)$$

where $\omega' = (\omega_z^2 - \beta^2)^{1/2}$. The peak velocity v_0 is then computed from the fitted A for each data subset to obtain the damping coefficient β as a function of v_0, with the results shown in Fig. 3. The damping monotonically increases for small v_0 and peaks near $v_0 \sim 1.1c_0$, followed by a nearly exponential decay of β for $v_0 > c_0$.

A perturbative theoretical treatment has produced a closed-form solution for the velocity-dependent damping, which results in good quantitative agreement with our measurements [40]. For weak disorder, the qualitative behavior shown
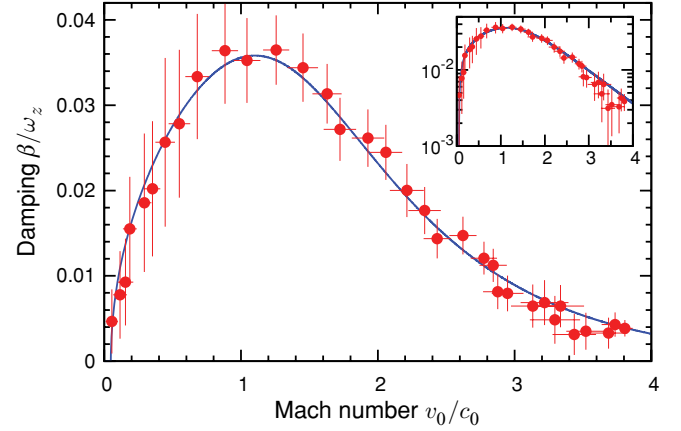

FIG. 3. (Color online) Velocity-dependent damping. Results of fitting the data of Fig. 2 to Eq. (5) by using a traveling four-period window. The peak velocity v_0 is obtained from $v_0 = A\omega_z$. The solid line is a square-root function convolved with an exponential decay and is meant as a guide to the eye. The inset shows the same data on a semilogarithmic plot, which emphasizes the nearly exponential decay of β/ω_z for large v_0/c_0. Vertical error bars correspond to the range in β for which $\Delta\chi^2 = 1$ for the fit to Eq. (5) while simultaneously adjusting A, β, and ϕ to minimize χ^2. Horizontal error bars are determined by using an identical process for A in Eq. (5) and are typically $\sim 15\%$. The effects of systematic uncertainty in imaging magnification and variations in N are $\sim 10\%$ in the horizontal axis and $\sim 5\%$ in the vertical axis; these are not included in the displayed error bars.

in Fig. 3 can be understood through a local Landau critical velocity argument. At low velocities, Bogoliubov quasiparticles are only created within a thin shell at the surface of the condensate, where the low density leads to a low local speed of sound, and, therefore, a low local v_L. As the velocity of the condensate increases, a larger condensate volume can support excitations because a larger fraction of the atoms violates the local Landau criterion. The maximum damping occurs near the point where the velocity of the BEC reaches the peak speed of sound c_0 in the condensate. At even larger velocities, the excitation volume cannot increase further, but the Bogoliubov density of states decreases, which results in the observed exponential decrease of the damping.

Except for the absence of a critical velocity, the qualitative behavior of the velocity-dependent damping shown in Fig. 3 is remarkably similar to that predicted by 1D NLSE simulations of a uniform repulsive BEC in the presence of an oscillating Gaussian obstacle [41,42]. In these simulations, above a certain impurity strength-dependent critical velocity, the impurity, which moves at a velocity v, deposits energy into the BEC in the form of density fluctuations. The average rate of condensate energy growth $\langle dE/dt\rangle$ increases nearly linearly with v, to a peak at $v \sim c$ as the defect excites dark solitons and linear sound waves. As the velocity of the defect is increased further, the density fluctuations decrease significantly, accompanied by an exponential decrease of $\langle dE/dt\rangle$, similar to our experimental observations. In contrast to a single impurity in a uniform condensate, a defect is always present in a low-density region of a condensate in a disordered harmonic trap. Consequently, v_0 is always greater than the local speed of
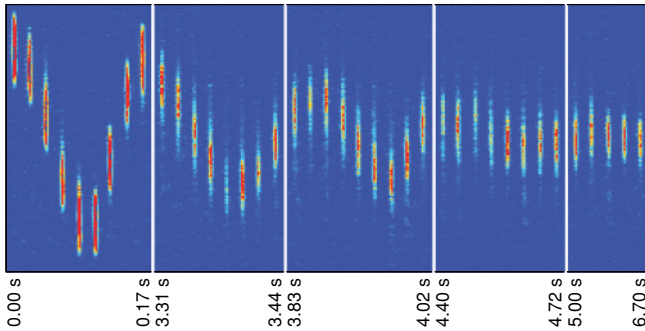
FIG. 4. (Color online) Characteristic *in situ* polarization phase-contrast images of the data shown in Fig. 2 at various times. The images are nearly equally spaced in time between the time labels.

sound at the edge of the condensate, and excitations are always present. Previous experimental [34,36,43] and numerical [44] studies of the damping of collective modes and the damping of Bloch oscillations in a disordered lattice potential [45,46] have found qualitatively similar results.

Figure 4 shows *in situ* polarization phase-contrast images [47] of the BEC at various times in the oscillation shown in Fig. 2. The damping clearly does not result from a loss of collectivity as predicted by 1D NLSE numerical simulations [44]. Rather, the BEC nearly maintains its original shape throughout the oscillation. Close inspection of the density distributions in Fig. 4 reveals a tail of noncondensed atoms that appears to oscillate slightly out of phase with the central Thomas-Fermi distribution. At early times, these noncondensed atoms appear to lag behind the BEC, while at later times, they oscillate in-phase with it. This two-component out-of-phase oscillation is reminiscent of the second sound-like oscillation reported in Ref. [48]. In that work, the initial temperature was high enough that damping occurred due to the interaction between a BEC and a thermal component. In contrast to those results, we observe that the dipole oscillation is undamped in the absence of the disordered potential. Furthermore, there is no observable heating due to the quick switch on of the disorder. In our experiment, therefore, the presence of the noncondensed component seems to be linked to the motion of the BEC in the disordered potential. A recent numerical simulation, which uses a truncated Wigner method, predicts the emission of incoherent atoms from a BEC moving supersonically through a disordered potential [49], consistent with our observations.

We have investigated this effect in further detail by using *in situ* absorption imaging, which allows for the determination of the low-density noncondensed wings of the distributions. Figure 5 shows that, by fitting the cloud to a bimodal Thomas-Fermi plus Gaussian profile, a phase difference of $\Delta\phi = 0.23$ between the condensed and noncondensed cloud centers is found. Note that the interaction strength is different for these data than for those data shown in Figs. 2–4.

We have systematically investigated the dependence of β on the disorder strength V_D. Figure 6 shows the normalized damping parameter β/ω_z plotted against the normalized disorder strength V_D/μ, where μ is the chemical potential of the condensate prior to the kick and before the disorder is
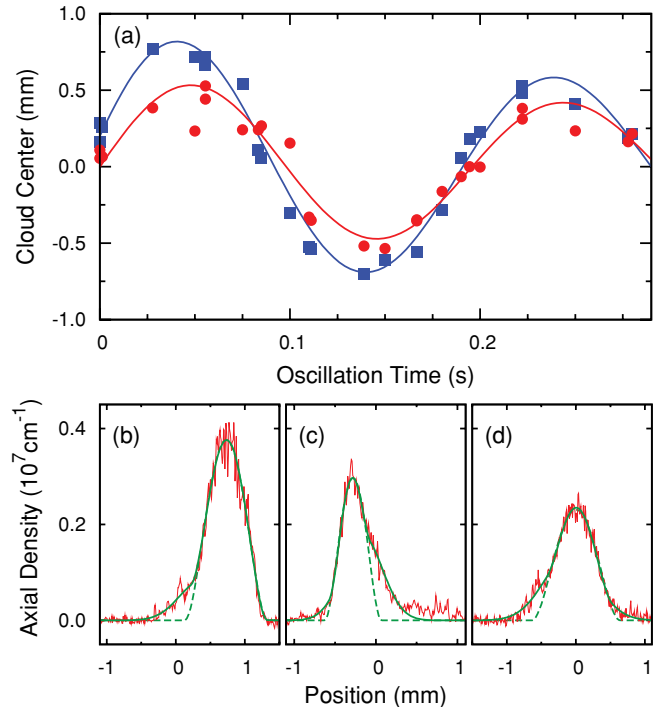

FIG. 5. (Color online) Generation of a noncondensed component. (a) Squares show the center of the Thomas-Fermi (condensed) component, and circles show the center of the Gaussian (noncondensed) component. The Gaussian center trails behind the Thomas-Fermi center and has a smaller amplitude of oscillation. Within experimental uncertainty, $\omega_z = 2\pi \times 5.1(2)$ Hz for both components. For these data, $a = 200\,a_0$, $N = 3 \times 10^5$, $\mu/h = 1.8$ kHz, $V_D/\mu = 0.22$, $v_0 = 28$ mm/s, $c_0 = 7.2$ mm/s, and $\omega_r = 2\pi \times 220$ Hz. (b)–(d) Axial density distributions with bimodal fits (solid lines) and a single-component Thomas-Fermi fit (dashed lines) at various times during the oscillation: (b) 28 ms, (c) 100 ms, and (d) 190 ms. The condensates in (b) and (d) are traveling in the positive direction, whereas the condensate in (c) is traveling in the negative direction.

switched on. We find the data fit well to a power law,

$$\frac{\beta}{\omega_z} \propto \left(\frac{V_D}{\mu}\right)^p \qquad (6)$$

for all measured velocities. The precise value of p, however, depends weakly on v_0 across the range of velocities $0 < v_0/c_0 < 5$, with a mean value of $p = 2.1(5)$ (see Fig. 6 inset).

Figure 7 presents the measured values of β as a function of both V_D and v_0. As expected, a vertical trace through this plot shows a qualitative similarity to Fig. 3. We observe two distinct regimes of reduced damping: one where $v_0/c_0 \ll 1$ and the other when $v_0/c_0 \gg 1$, where the damping reaches a maximum at $v_0 \sim c_0$. A numerical simulation that uses an effective 1D NLSE has produced qualitatively similar results [44].

B. Variation with interaction strength

We observe nearly universal behavior for β as a function of both V_D/μ and v_0/c_0 for BECs in the Thomas-Fermi regime. As already shown in Fig. 6, $\beta \propto (V_D/\mu)^2$ for condensates with values of μ that differ by a factor of 3. Shown in Fig. 8 is a comparison between the damping at interaction strengths
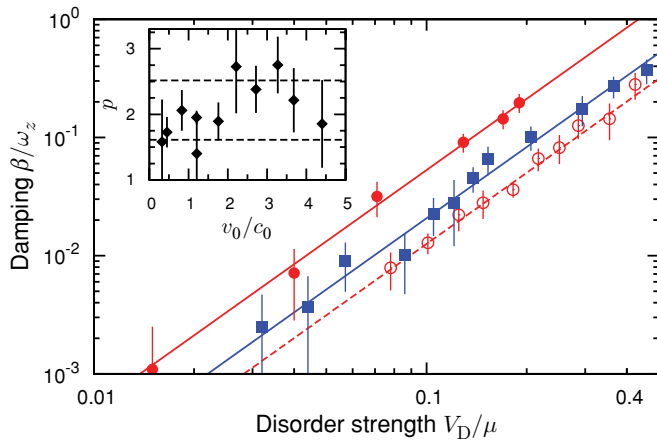
FIG. 6. (Color online) Damping vs V_D. Open circles correspond to the data shown in Fig. 7 ($a = 200 \, a_0$) in the range $0.7 < v_0/c_0 < 0.9$; filled circles correspond to $a = 200 \, a_0$, $v_0/c_0 = 1.2$, $\mu/h = 2.2$ kHz; squares correspond to $a = 25 \, a_0$, $v_0/c_0 = 1.2$, $\mu/h = 750$ Hz. The damping parameter β follows a power law with $p \sim 2$ (solid and dashed lines), independent of μ or a. To minimize systematic effects associated with the velocity dependence of β (e.g., Figs. 2 and 3), we fit a four-period window for which the data are described well by Eq. (5). Vertical error bars are as defined in Fig. 3. The inset shows the fit values of p as a function of v_0/c_0 for a collection of data sets at $a = 200 \, a_0$. The dashed lines indicate the plus-and-minus one standard deviation extent for the collection of measured velocities. Vertical error bars for p are determined as in Fig. 3 by using a fit to Eq. (6) for each oscillation at a given v_0/c_0. Data that correspond to filled circles and squares were taken by using an optical trap setup different from that described in Sec. II with $\lambda = 1064$ nm and a beam waist of 24 μm, which results in $\omega_z = 2\pi \times 4.9$ Hz, $\omega_r = 2\pi \times 460$ Hz, and $N = 3 \times 10^5$. Also, for these data sets, $\sigma_D = 3.4 \, \mu$m.

$a = 200 \, a_0$ and $a = 28 \, a_0$, with constant V_D/μ. Although the respective values of c_0 differ by nearly a factor of 2 between the two data sets, the peak damping occurs at $v_0/c_0 \sim 1$ for both, which demonstrates the nearly universal behavior of β vs v_0/c_0. On the other hand, the peak damping rate between the two data sets differs by nearly a factor of 5, which shows that while the general shape of the damping curve is universal, the magnitude of the damping is not.

An investigation of the effect of interatomic interactions on the peak damping ($v_0/c_0 \sim 1$) at fixed V_D/μ is shown in Fig. 9. We find that β scales linearly with a, going to zero with decreasing interactions, consistent with the disappearance of the low-energy phonon portion of the excitation spectrum as $U \to 0$.

The elongated confinement geometry in our system facilitates the investigation of the dimensional crossover from the 3D to the quasi-1D regime where $\mu \ll \hbar\omega_r$ [50,51]. Shown in Fig. 10 are measurements of β vs μ at constant V_D and v_0. When $\mu > \hbar\omega_r$ (to the right of the vertical dashed line) and v_0 is comparable to, or less than c_0 (as is the case for the data shown as open and closed circles), we find $\beta \propto \mu^{-1.4}$. With reference to Fig. 7, one can gain a qualitative understanding of the behavior of the system going from high to low μ: when starting subsonically (open and filled circles), the system travels along a path from the weakly damped regime (lower
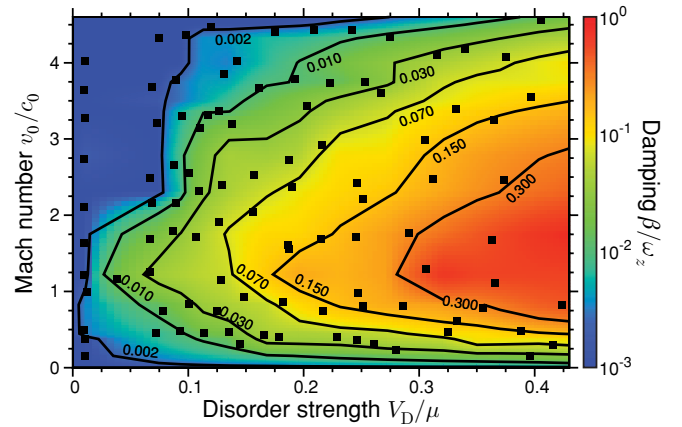

FIG. 7. (Color) Transport regimes of a BEC that travels through a disordered harmonic potential. Black squares show the values of disorder strength V_D/μ and initial peak c.m. velocity v_0/c_0 for the data used to extract β from a fit to Eq. (5) by using four to six periods of oscillation. The interpolated color map and contour lines for β/ω_z are derived from the measured results. These measurements have $a = 200 \, a_0$, $N = 2 \times 10^5$ atoms, $\mu/h = 1.5$ kHz, $c_0 = 6.5$ mm/s, $\omega_r = 2\pi \times 260$ Hz, and $\omega_z = 2\pi \times 5.5$ Hz. The variable experimental quantities are A and V_D. Due to small shot-to-shot fluctuations in the position of the c.m. of the cloud, measurements with $v_0 < 0.2c_0$ are not reliable. Data with $\beta \leqslant 2 \times 10^{-3}$ are consistent with undamped motion.

left corner of Fig. 7) toward the regime of strong damping (middle right region). As μ decreases, the quantities V_D/μ and v_0/c_0 increase correspondingly, and the system follows a path that crosses several contours of constant β while approaching the strongly damped regime near $v/c \sim 1$. Consequently, the system displays a strong dependence of β on μ. Blue squares depict a different situation where the system is supersonic for all μ investigated. For large μ, the system occupies a
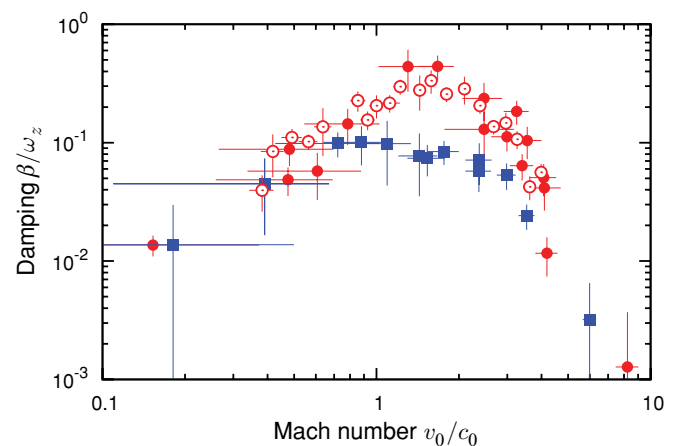

FIG. 8. (Color online) Universal damping vs v_0/c_0. The disorder strength was adjusted to keep $0.30 < V_D/\mu < 0.35$ for all of the data. Squares correspond to $a = 28 \, a_0$, $N = 2.5 \times 10^5$, $\mu/h = 550$ Hz, $c_0 = 4.0$ mm/s, $\omega_z = 2\pi \times 5.5$ Hz, and $\omega_r = 2\pi \times 260$ Hz; open circles correspond to $a = 200 \, a_0$, $N = 3 \times 10^5$, $\mu/h = 2.4$ kHz, $c_0 = 8.3$ mm/s, $\omega_z = 2\pi \times 4.5$ Hz, and $\omega_r = 2\pi \times 460$ Hz; filled circles correspond to the same parameters as in Fig. 7. Error bars are as defined in Fig. 3.
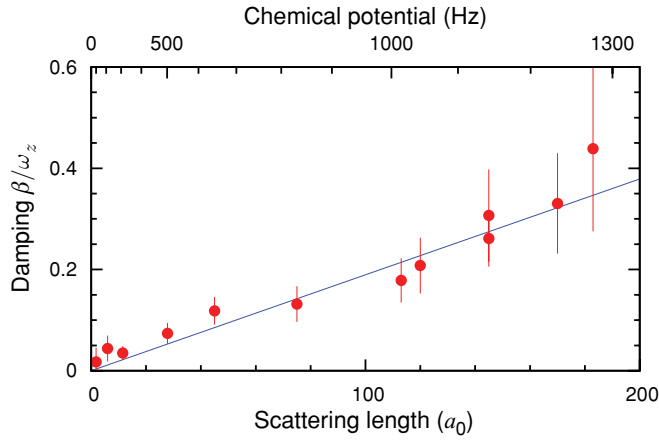
FIG. 9. (Color online) Peak damping vs a with fixed V_D/μ and v_0/c_0. For these data, V_D and v_0 were adjusted to keep $0.3 < V_D/\mu < 0.4$ and $0.6 < v_0/c_0 < 1.4$ with all other parameters as in Fig. 7. The upper horizontal axis shows values for μ obtained from a variational solution of the GPE [21] (note that the upper tick marks are not strictly logarithmically spaced). The linear fit has a slope $0.002a_0^{-1}$. Vertical error bars are as defined in Fig. 3.

FIG. 10. (Color online) Damping vs μ with fixed V_D and v_0. Squares and filled circles correspond to $V_D/h = 370$ Hz with $v_0 = 11$ and 6 mm/s, respectively. Open circles correspond to $V_D/h = 140$ Hz and $v_0 = 6$ mm/s. The vertical dashed line denotes $\mu = \hbar\omega_r$, at which point, $v_0/c_0 = 1.7$ for the open and filled circles and $v_0/c_0 = 3$ for the squares. We varied μ by adjusting a, shown on the upper horizontal axis (note that the upper tick marks are not strictly logarithmically spaced). Values for μ are obtained from a variational solution of the GPE [21] using the following measured experimental parameters: $\omega_r = 2\pi \times 460$ Hz, $\omega_z = 2\pi \times 4.5$ Hz, and $N = 4 \times 10^5$ atoms. For this data, $\sigma_D = 3.4$ μm. Vertical error bars are as defined in Fig. 3.

point in Fig. 7 with $v_0/c_0 > 1$ and $V_D/\mu < 1$. As μ decreases, the system follows a diagonal path, roughly tracing a contour line of constant β, moving into the regime of $v_0/c_0 \gg 1$ and $V_D/\mu \gg 1$ (top-right corner of Fig. 7). When $\mu < \hbar\omega_r$ (to the left of the vertical dashed line) and $v_0 \gg c_0$, we observe a negligible dependence of β on μ. In this quasi-1D regime, β is affected only by changing V_D or v_0, consistent with the behavior expected for a nearly ideal classical fluid. This may be understood with reference to Eq. (2) where, for $v \gg c$, the first term in the Bogoliubov excitation spectrum dominates making the system quasi-ideal with $\epsilon(p)$ independent of μ.

Figure 11 shows damping of a weakly interacting gas with $a = 0.4\,a_0$, deep into the quasi-1D regime, where $\mu/\hbar\omega_r \sim 0.1$. We find that $V_D = 4\mu$ produces the same damping ($\beta/\omega_z = 0.07$) as that for a BEC with $a = 200\,a_0$ and $V_D = 0.25\mu$. The nature of the damped motion of a weakly interacting gas in strong disorder is strikingly different from the damped motion of a strongly interacting gas in weak disorder, although the timescale of the damping in both cases is comparable. Figure 11 shows that the damping in the weakly interacting regime is caused by the loss of coherence of the collective dipole mode brought on by extensive fragmentation. Because $V_D > \mu$, it is perhaps not surprising that the condensate quickly fragments. While the c.m. of the cloud damps after about five oscillation periods, examination of shot-to-shot differences in the damped density distributions reveal that the positions of the fragments are highly nonrepeatable, which suggests that some fragments remain in motion. This residual motion is consistent with the long thermalization time expected from weak two-body interactions. It is interesting to note that the maximum single-particle kinetic energy $E_K = \frac{1}{2}m\omega_z^2 A^2 = h \times 295$ Hz is 2.8 times larger than the average height of the disordered potential. Therefore, the observed dephasing is consistent with the expected behavior of a gas of noninteracting particles that are interacting with a disordered potential where the disorder
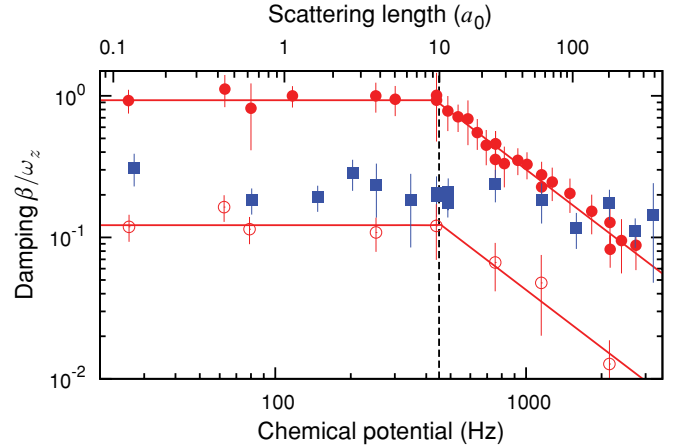
strength is smaller than the kinetic energy of the individual particles.

IV. DISSIPATION INDUCED BY A SINGLE GAUSSIAN DEFECT

A. Thomas-Fermi regime

In an effort to better understand the mechanisms responsible for the damping by disorder, we have investigated the dissipation induced by a *single* Gaussian defect. The defect potential is described by $V(z) = V_D e^{-2z^2/w_z^2}$, where $w_z = 12$ μm. The static effect of either an attractive or a repulsive defect on a repulsively interacting BEC in the Thomas-Fermi regime is shown in Fig. 12. As expected, the attractive defect leads to an increase in the density in the region of the defect, accompanied by a small decrease in the density in the wings of the distribution, while the opposite is true for a repulsive defect.

The dynamical distributions can differ dramatically from the static case, as shown in Fig. 13 where *in situ* axial densities are displayed for various times throughout the dipole oscillation. In the following discussion, we refer to the upstream side of the condensate as the portion of the BEC that reaches the barrier after the leading or downstream portion. The interaction of the BEC with the repulsive defect, shown in Fig. 13(b), produces a deep downstream density rarefication as well as a large upstream density compression, which bears a qualitative similarity to a shock wave. Similar structures have been predicted in effective 1D theoretical treatments [30,52] and interpreted as upstream and downstream dispersive shocks. In contrast, the interaction of the BEC with the attractive defect,
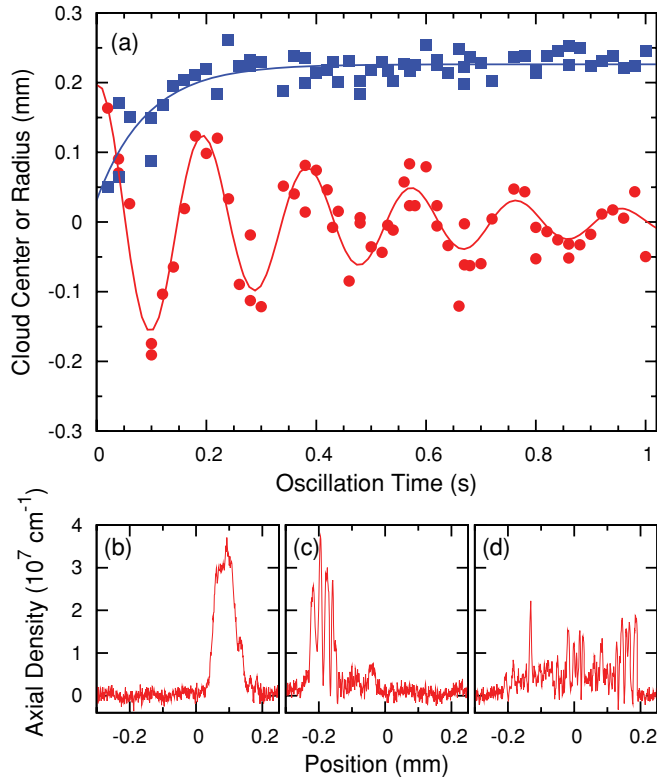
FIG. 11. (Color online) Damping of a nearly noninteracting gas. For this data, $a = 0.4\,a_0$, $N = 2 \times 10^5$, $\mu/h = 26$ Hz, $c = 1.2$ mm/s, $V_D = 4\mu$, $\omega_r = 2\pi \times 240$ Hz, and $\omega_z = 2\pi \times 5.3$ Hz. (a) C.m. position (circles) and radius (squares) of the condensate as a function of time. Here, we use statistically determined values for the c.m. $z_{\rm cm} = \int zn(z)\,dz/N$ and radius R, given by $R^2 = 4\int(z - z_{\rm cm})^2 n(z)\,dz/N$. (b)–(d) Axial density traces at various times in the oscillation: (b) 40 ms (c) 100 ms, (d) 960 ms. After two full oscillations, the cloud has fragmented and has spread to a size comparable with the initial oscillation amplitude.

shown in Fig. 13(a), produces no such shock waves. However, the cloud is slightly compressed near the defect simply due to the attractive defect potential. Because $v_0 > c_0$, phonon excitations cannot be emitted in the upstream direction as they would have to propagate faster than the speed of sound. Close inspection of Fig. 13(a) reveals minimal density modulation of the upstream side, while more modulation is evident on the downstream side.

Several 1D theoretical studies predict the formation of downstream propagating dark solitons in addition to an upstream dispersive shock as a repulsive defect is supersonically swept through a condensate [30,42,44,52–56], which is consistent with the density fluctuations visible in Fig. 13. However, the size of the dark solitons will be on the order of the healing length $\xi = 0.5\,\mu$m for these condensates, which is a factor of 6 smaller than our imaging resolution.

Figure 14 shows time-of-flight images of the BEC, which oscillate in the presence of a single repulsive defect. In contrast to the *in situ* images of Fig. 13(b), after time-of-flight, additional structures emerge, which were not previously visible. These structures are consistent with dark solitons that form from short length-scale *in situ* phase fluctuations that map onto larger-scale density modulations after time-of-flight.
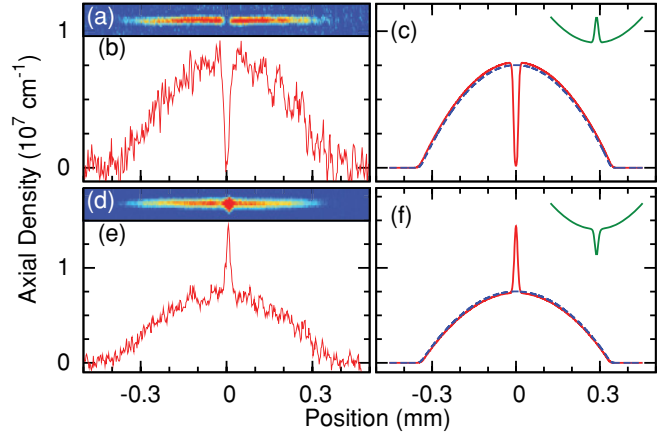

FIG. 12. (Color online) BEC in a harmonic trap with a single Gaussian defect. (a)–(c) correspond to a repulsive defect, while (d)–(f) correspond to an attractive one. (a) and (d) *In situ* polarization phase-contrast images, (b) and (e) axial densities, which correspond to the images, and (c) and (f) numerical solutions to the GPE with the dashed lines that show the solution in the absence of a defect. The inset trace shows the characteristic shape of the potential. For all panels, $a = 200\,a_0$, $N = 4 \times 10^5$, $\omega_z = 2\pi \times 5.0$ Hz, and $\omega_r = 2\pi \times 360$ Hz.

However, *in situ* phase fluctuations may also arise from thermal excitations in highly elongated BECs, and these can also manifest as density fluctuations after time of flight [57]. Close inspection of Fig. 14 reveals that deep density modulations are present only in the downstream portion of the BEC (after the first pass through the defect), consistent with the dark soliton interpretation. Similar density fluctuations have also been interpreted as dark solitons in an experiment by using a moving defect and a stationary BEC [58].
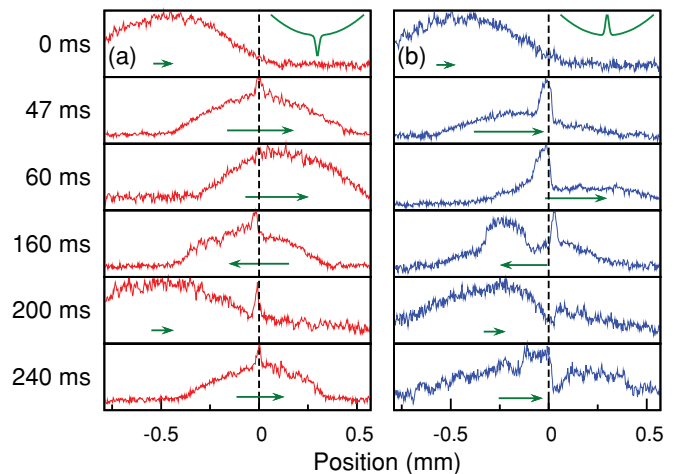

FIG. 13. (Color online) Axial densities at various times during a supersonic oscillation in the presence of (a) an attractive or (b) a repulsive defect. The arrows are proportional to the instantaneous velocity of the condensate. The vertical dashed lines denote the location of the defect. For these data, $a = 200\,a_0$ and $v_0 = 13$ mm/s; (a) corresponds to $N = 4 \times 10^5$, $\mu = 1.5$ kHz, $v_0/c_0 = 2$, $V_D = -0.8\mu$, $\omega_z = 2\pi \times 4.7$ Hz, and $\omega_r = 2\pi \times 360$ Hz; (b) corresponds to $N = 1 \times 10^6$, $\mu = 3$ kHz, $v_0/c_0 = 1.4$, $V_D = 0.4\mu$, $\omega_z = 2\pi \times 5.0$ Hz, and $\omega_r = 2\pi \times 360$ Hz.
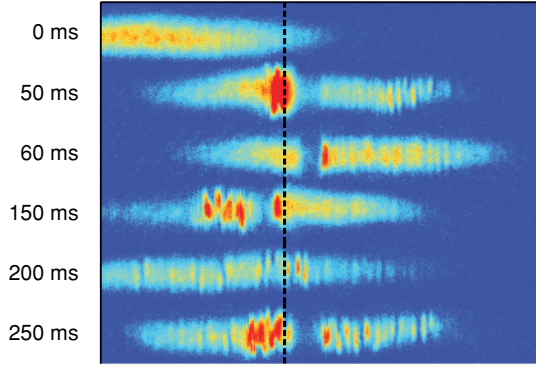
FIG. 14. (Color online) Density fluctuations produced, which cross a repulsive defect. Absorption images after 4-ms time of flight. The vertical dashed line denotes the location of the defect. The experimental parameters are as stated in Fig. 13(b).

We have measured β as a function of both V_D and v_0, with characteristic results presented in Fig. 15. Contrary to what was observed for a disordered potential, we observe a critical velocity v_c below which the motion is undamped for both the attractive and the repulsive defects. We find that the peak damping for an attractive defect is significantly weaker than for a repulsive one. Figure 16 presents measurement results of β as a function of both V_D and v_0. For an attractive defect, we find that $v_c/c_0 \sim 0.7$ where v_c depends only weakly on V_D. However, for a moderately strong repulsive defect, v_c/c_0 occurs significantly below 1 and depends strongly on V_D. For both attractive and repulsive defects, v_c tends to c_0 as $|V_D/\mu|$ is reduced to zero.

Once again, a model based on a local Landau criterion is sufficient to explain the dependence of v_c on V_D. For simplicity, consider a uniform density flow that impinges on either a repulsive or an attractive Gaussian potential [54]. With the assumption that the superfluid flow pattern is stationary, the local density of the condensate near the defect must be modified in a similar way to that shown in Fig. 12 for
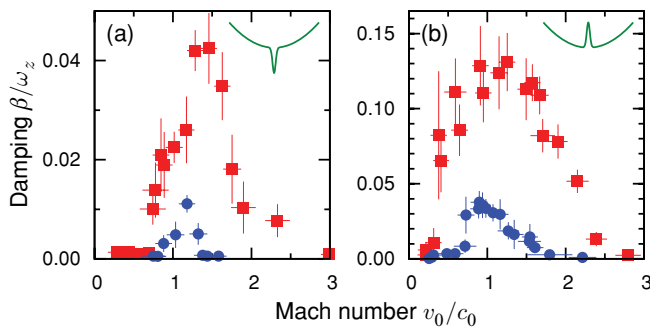

FIG. 15. (Color online) Velocity dependence of β induced by a single Gaussian defect. (a) Attractive defect with (squares) $V_D/\mu = -0.8$ or (circles) $V_D/\mu = -0.3$ and other parameters as stated in Fig. 13(a) except with $N = 8 \times 10^5$ and $\mu/h = 2$ kHz. (b) Repulsive defect with (squares) $V_D/\mu = 0.4$ or (circles) $V_D/\mu = 0.2$ and other parameters as stated in Fig. 13(b). Both types of impurities show critical behavior at low velocities as well as undamped motion at large v_0/c_0. Note the difference in scale between damping induced by an attractive vs a repulsive impurity. Vertical and horizontal error bars are as described in Fig. 3.
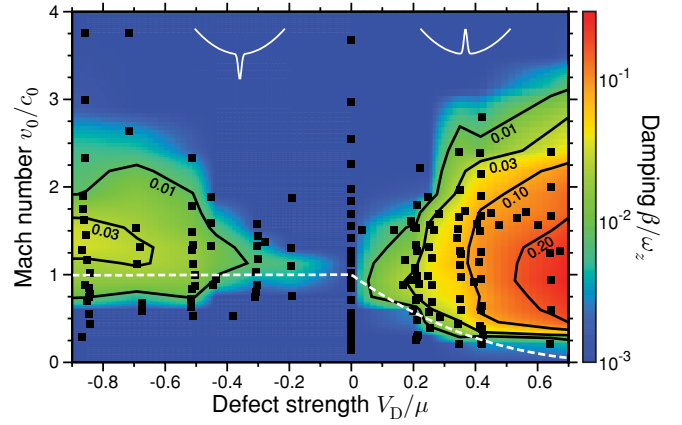

FIG. 16. (Color) Transport regimes of a BEC that travels through a harmonic potential with a central Gaussian defect. Coordinates of the black squares are the values of V_D/μ and v_0/c_0 for the data sets used to extract β/ω_z from a fit to Eq. (5). The interpolated color map and contour lines for β/ω_z are derived from the measured results. Dashed white lines show the local Landau critical velocity as given by Eqs. (7) and (9). The attractive and repulsive cases are qualitatively similar: superfluidity for $v_0/c_0 \ll 1$, increased damping as $v_0/c_0 \to 1$, and reduced damping for $v_0/c_0 \gg 1$. Damping induced by an attractive impurity is an order of magnitude weaker than for a repulsive one. Data with $V_D < 0$ and $V_D > 0$ correspond to parameters in Figs. 13(a) and 13(b), respectively.

a static defect. For the repulsive case, the local density is reduced near the defect, which results in a lower local speed of sound. In addition, flux conservation requires that the local condensate velocity increase in the low-density region near the repulsive impurity to preserve the stationary flow pattern. A corresponding argument can be made for the case of an attractive defect. These effects serve to increase the local value of $v(z)/c(z)$ near a repulsive defect and decrease it for an attractive one. As a result, excitations can be created near the peak of the repulsive defect in a BEC with a c.m. velocity that is significantly lower than the bulk speed of sound. For the case of an attractive impurity, on the other hand, one expects excitations to occur in the bulk condensate first, rather than near the impurity, and, therefore, at a flow velocity near the bulk speed of sound, as observed.

We quantify this picture, in the case of a repulsive defect, by applying the local Landau criterion at the instant the center of the BEC crosses the defect. In Ref. [44], the authors used an effective 1D NLSE in the high-density regime to determine the locus of points where the local condensate velocity $v(z)$ is equal to the local speed of sound $c(z)$; this defines the curve,

$$\frac{v_c}{c_0} = \left(1 - \frac{V_D}{\mu}\right)^{5/2}, \qquad V_D > 0, \qquad (7)$$

where $V_D/\mu \equiv \delta n_0/n_0$ is the fractional change in the peak density at the peak of the repulsive defect. When $v_0/c_0 < 1$, we can ignore effects of the axial Thomas-Fermi profile of the condensate because $A \ll R_{TF}$ for our trap, where R_{TF} is the axial Thomas-Fermi radius. Equation (7) is plotted in Fig. 16 when $V_D > 0$ and is found to agree with the measured v_c for the range of V_D explored experimentally. Therefore, the observed reduction of the critical velocity below c_0 is

consistent with the *local* Landau critical velocity without invoking more exotic mechanisms, such as vortex nucleation. This is in contrast with several experiments that involve BECs in less elongated configurations [6,7], as well as in superfluid ^{4}He where nucleation of vortex lines and rings can result in $v_c < v_L$ [25].

In the case of the attractive defect, the density and, therefore, $c(z)$ are enhanced at the location of the defect and reduced only slightly elsewhere. We find that the reduction in density in the bulk due to the enhancement at the defect is less than 1% for the strongest barriers used, which leads to an essentially unperturbed speed of sound in the bulk. The ratio of the local fluid velocity to the local speed of sound can then be found by only considering the bare Thomas-Fermi profile, and is given by

$$\frac{v(z)}{c(z)} = \frac{v_0}{c_0}\left(\frac{1 - z^2/A^2}{1 - z^2/R_{\mathrm{TF}}^2}\right)^{1/2}, \qquad (8)$$

where, by using Eq. (4), $v_0/c_0 = 2A/R_{\mathrm{TF}}$. If $2A < R_{\mathrm{TF}}$, then $v_0/c_0 < 1$, and the local Landau criterion is satisfied everywhere inside the condensate,

$$\frac{v_c}{c_0} = 1, \qquad V_D < 0, \qquad (9)$$

which implies that v_c is independent of V_D. Our measurements, however, show that v_c depends weakly on V_D with $v_c/c_0 \to 1$ only in the weak impurity limit. Our experimental results are consistent with numerical simulations that use a 1D NLSE [44] for which the local Landau criterion accurately describes the repulsive impurity case but slightly overestimates v_c in the attractive case.

Figures 15 and 16 demonstrate that damping is significantly suppressed deep into the supersonic regime. We observe undamped motion when v_0 is greater than a V_D-dependent upper critical velocity v_+. Numerical simulations [42,44,59] have shown that, for wide and smooth barriers ($\xi \ll w_z$), the emission of radiation from the defect in the form of phonons and solitons can be very small for supersonic velocities. In fact, it has been shown analytically that the radiation emission rate resulting from a defect moving supersonically through a condensate decreases exponentially with the ratio ξ/w_z [60]. Without emission of radiation, energy dissipation is inhibited and the flow persists, even though Landau's criterion is violated. For the data presented in Figs. 12–17, $\xi/w_z \sim 0.04$, well within the regime where supersonic nondissipative flow is predicted. Experiments similar to ours have also shown a reduction in soliton emission from a barrier that moves through a condensate in the supersonic regime [58].

Therefore, we observe three distinct regimes of flow in the single-defect system: subsonic superfluid ($v_0/c_0 < 1$), dissipative ($v_0/c_0 \sim 1$), and supersonic nondissipative ($v_0/c_0 > v_+$). Figure 17 displays axial densities from *in situ* polarization phase-contrast images at the instant the defect passes through the peak of the condensate for the three different velocity regimes. As expected, for the superfluid flow regime, the axial density profiles look very much like the equilibrium profiles of Fig. 12: there is an increase (decrease) in the density at the location of the attractive (repulsive) defect. In the dissipative flow regime, on the other hand, the flow
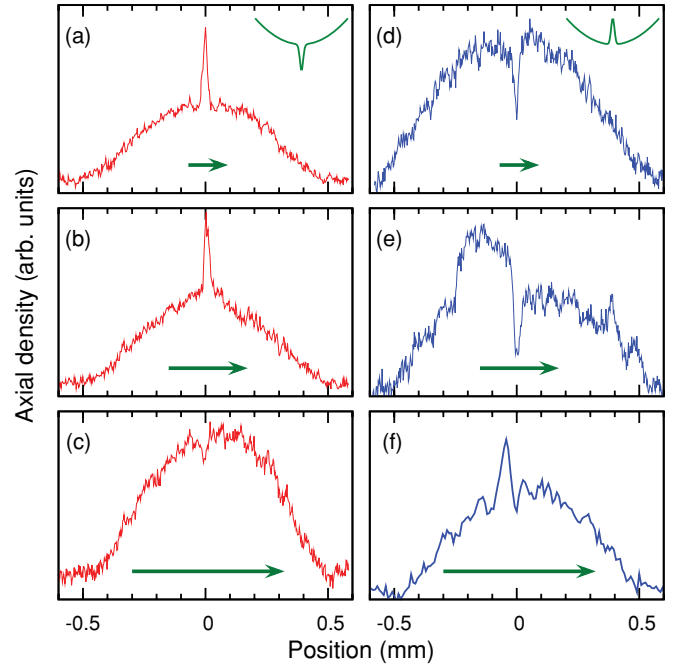

FIG. 17. (Color online) *In situ* density distributions of a condensate that passes through a Gaussian defect. These images are taken at the instant the center of the BEC first crosses the defect. Rows correspond to the three flow regimes: subsonic superfluid ($v_0/c_0 < 1$), dissipative ($v_0/c_0 \sim 1$), and supersonic nondissipative ($v_0/c_0 > 1$). (a)–(c) Attractive defect with $V_D/\mu = -0.85$ and $v_0/c_0 = 0.31$, $v_0/c_0 = 1.0$, and $v_0/c_0 = 3.0$, respectively. (d)–(f) Repulsive defect with $V_D/\mu = 0.65$ and $v_0/c_0 = 0.15$, $v_0/c_0 = 0.90$, and $v_0/c_0 = 2.0$, respectively. The arrows indicate the direction and the relative speed of the condensate. For these data, all other parameters are as described in Fig. 13.

patterns for $V_D > 0$ show significant distortion, while for $V_D < 0$, there is little distortion, as previously discussed in detail. Finally, in the supersonic nondissipative flow regime, we observe a counterintuitive density *inversion* with respect to the superfluid regime, where the attractive defect produces a density depression, while the repulsive defect causes a density peak.

The physical origin of this counterintuitive density inversion can be understood by considering the behavior of the gas at large v_0. In this regime, as in the disordered case, the Bogoliubov excitation spectrum, given by Eq. (2), is dominated by the $p^2/2m$ term and, therefore, is dominated by plane waves with wave number $k = p/\hbar$ rather than phonons. For this quasi-ideal gas, the drag should be determined by the scattering of these plane waves off of the defect [54]. At high velocities, scattering of these waves from the defect is greatly suppressed, which leads to low dissipation. If we extend this argument further and if we consider the atoms to be classical particles, one expects the atoms to slow down in the presence of the repulsive defect, which results in a density increase near the defect, while the opposite is expected for an attractive defect.

Density inversions similar to the ones presented here have also been discussed in the context of dissipationless stationary states at supersonic velocities [53,60–62] as well as sonic
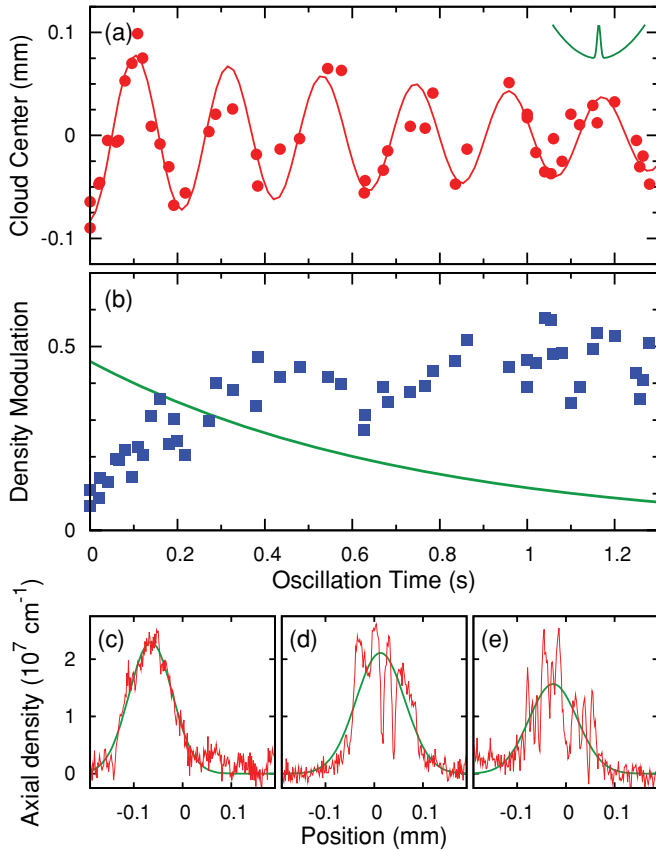
FIG. 18. (Color online) Oscillation of a weakly interacting BEC in the presence of a repulsive defect, with $a = 0.6\,a_0$, $N = 2.5 \times 10^5$, $\mu/h = 44$ Hz, $V_D/\mu = 0.8$, $\omega_z = 2\pi \times 4.7$ Hz, $\omega_r = 2\pi \times 300$ Hz, and $v_0/c_0 = 1.6$. (a) C.m. position as a function of time (computed as in Fig. 11), we find $\beta/\omega_z = 0.03$, (b) root-mean-square density deviation from a Gaussian fit to the axial density distribution (see text). The solid line shows the decay of the oscillation energy (in arbitrary units) found from the fit in (a). (c)–(e) *In situ* axial density traces and Gaussian fits at various oscillation times: (c) 0 ms, (d) 140 ms, at the second crossing of the defect, and (e) 1260 ms, after several crossings of the defect. At increasingly large times, we find that the large density modulations are accompanied by only a slight increase of the axial size of the condensate.

black holes [63]. Under our experimental conditions, when $v_0/c_0 \sim 1$, the edge of the barrier can serve as a sonic event horizon. Such systems have been proposed as possible candidates with which to study tabletop astrophysics, where exotic effects, such as Hawking radiation, should be observable. Interestingly, in this system, the experimenter plays the role of the so-called superobserver, by having access to the regions both outside and *inside* the event horizon [63–66].

B. Weakly interacting regime

Figure 18 shows results of measurements of a weakly interacting condensate ($a = 0.6\,a_0$), which oscillates in the presence of a repulsive defect. Under these conditions, the condensate is in the quasi-1D regime with $\mu/\hbar\omega_r = 0.15$. We find that the axial density profile of the condensate becomes increasingly modulated during the damped oscillation, consistent with theory [42,55]. We compute the root-mean-square
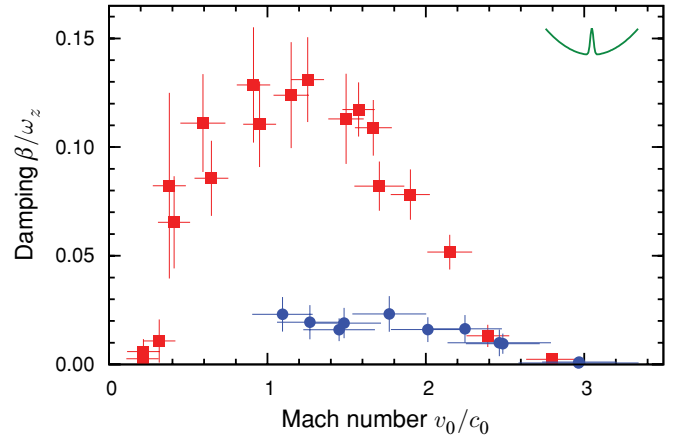

FIG. 19. (Color online) Velocity dependence of damping with a repulsive defect. Circles correspond to a nearly noninteracting BEC with $a = 0.6\,a_0$, $\mu/h = 31$ Hz, $c_0 = 0.9$ mm/s, and $V_D = 0.9\mu$. Shot-to-shot variations in the position of the cloud limit the extraction of β to $v_0 > 1$ mm/s, which corresponds to $v_0/c_0 > 1.1$. Squares correspond to data from Fig. 15(b) for comparison, $a = 200\,a_0$, $\mu/h = 3$ kHz, $c_0 = 9.2$ mm/s, and $V_D = 0.4\mu$. Error bars are as defined in Fig. 3.

deviation of the axial density distribution from a Gaussian fit n_{fit} as a proxy for the increased internal energy of the condensate due to the density modulation,

$$\Delta = \sqrt{\frac{1}{L}\int_L \left[\frac{n(z) - n_{\text{fit}}(z)}{n_{\text{fit}}(z)}\right]^2 dz}, \qquad (10)$$

where we take the integration length L to be over the central 70% of the condensate to minimize edge effects. Figure 18(b) shows that Δ initially increases in time and then saturates. The time-dependent increase in the density modulation qualitatively matches the loss of oscillation energy. Therefore, we conclude that the damping of the dipole mode is caused primarily by the creation of *in situ* density modulations in the cloud.

Results of measurements of the velocity dependence of the damping by a repulsive defect with $a = 0.6\,a_0$ are shown in Fig. 19. As was the case with disordered potentials, we find that the timescale for damping in the quasi-1D regime with a strong impurity strength is much longer than that observed in the Thomas-Fermi regime with a weak impurity strength.

C. Dark soliton production in the weakly interacting regime

Of particular interest in the quasi-1D regime is the ability to create and to observe long-lived dark solitons. These nonlinear excitations have been previously created in BECs with repulsive interatomic interactions through a variety of means, which include direct phase imprinting [67,68], spatially selective microwave transfer [69], slow light [70], two-condensate interference [71,72], and, similar to the work presented here, as a result of a BEC crossing a semipermeable defect [58].

In general, the decay of dark solitons occurs as a result of dynamical instability or as a result of dissipative dynamics associated with the interaction of the soliton with quasiparticle excitations of the BEC. However, it is known that dark solitons
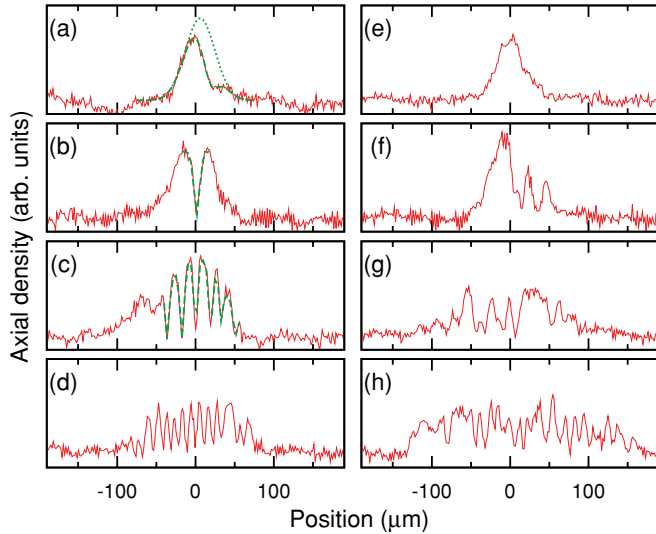
FIG. 20. (Color online) Dark soliton formation. *In situ* axial densities of BECs during the first (a)–(d) and fourth (e)–(h) passes through a semipermeable defect. The defect is located at $z = 0$, and its strength was adjusted to keep $V_D/\mu \sim 0.7$. Oscillation amplitudes were adjusted to keep $v_0 \sim c_0$. (a), (e): $a = 0.1\,a_0$, $N = 1.0 \times 10^5$, $\mu/h = 5$ Hz, $\xi = 12.5$ μm, $\xi_s = 16(6)$ μm; (b), (f): $a = 0.5\,a_0$, $N = 2.2 \times 10^5$, $\mu/h = 30$ Hz, $\xi = 4.9$ μm, $\xi_s = 6.6(2)$ μm; (c), (g): $a = 1.7\,a_0$, $N = 2.6 \times 10^5$, $\mu/h = 77$ Hz, $\xi = 3.06$ μm, $\xi_s = 2.8(4)$ μm; (d), (h): $a = 5.4\,a_0$, $N = 2.2 \times 10^5$, $\mu/h = 144$ Hz, $\xi = 2.24$ μm, $\xi_s = 2.5(3)$ μm. The trap frequencies for these data are $\omega_r = 2\pi \times 240$ Hz and $\omega_z = 2\pi \times 4.75$ Hz. The dashed lines show fits to Eq. (11). We omit the fit in (d) for clarity. For comparison, the thin dashed line in (a) is only the Gaussian portion of the fit. Error bars for ξ_s are given by the standard deviation of a collection of images.

can have very long lifetimes in the quasi-1D regime [73]. For the most weakly interacting BECs presented here, $\mu/\hbar\omega_r = 0.13$, thereby making our system ideally suited to study long-lived dark solitons.

We have studied the formation of deep *in situ* density modulations in BECs for different values of a, with the results shown in Fig. 20. Dipole motion is initiated after the field is slowly ramped to a desired value near the scattering length zero-crossing at 544 G. Panels (a)–(e) of Fig. 20 show the cloud after 3/4 of a complete oscillation. The defect is switched off after the first pass of the cloud, and the cloud is imaged after it returns to the center of the trap after another quarter period. Therefore, $\sim$100 ms elapses between the initial interaction of the cloud with the defect, where the soliton is created, and imaging. Deep density modulations, consistent with the formation of stable dark solitons, are observed. For comparison, panels (e)–(h) of Fig. 20 show the cloud after it passes through the defect four times. The density modulations in this case appear less monochromatic than in the single-pass case, which suggests the presence of both linear (phonons) and nonlinear (solitons) excitations. We extract the healing length ξ_s by fitting the single-pass data in Fig. 20 to [74]

$$n(z) = A e^{-z^2/\sigma^2} \left[1 - D\,\text{sech}^2 \left(\frac{z - z_0}{\xi_s \sqrt{2}} \right) \right], \quad (11)$$

where A is the background density, σ is the size of the atomic cloud, D is the depth of the soliton, z_0 is the location of the soliton, and ξ_s is the healing length. Through a variational solution of the GPE, we can independently estimate the healing length ξ by using the measured values of N, a, ω_z, and ω_r. The results of this analysis are reported in Fig. 20. The average size of the density dips is very nearly the healing length predicted by the GPE estimations (i.e., $\xi_s \sim \xi$). This observation is consistent with the formation of a downstream dispersive shock, which consists of a train of dark solitons as a supersonic BEC crosses a semipermeable barrier [42,44,53–56].

V. SUMMARY AND FUTURE DIRECTIONS

We have conducted comprehensive measurements of the dissipation of superfluid flow in an elongated BEC subject to either a disordered potential or a single Gaussian defect. By measuring the velocity and disorder strength-dependent damping parameter, we have characterized the breakdown of superfluidity of a harmonically trapped cloud in both the 3D Thomas-Fermi and the quasi-1D weakly interacting regimes.

Our data largely support the validity of the Landau criterion for a critical velocity above which the superfluid motion is damped, as long as the criterion is applied *locally*. The local criterion accounts for the inherent inhomogeneity of trapped gases, as well as density modifications produced by large defects. The only exception is for relatively strongly attractive defects, where we find that v_c decreases to $v_c \sim 0.7c_0$ for $V_D/\mu < -0.5$. Dissipation is also found to diminish for velocities greater than v_+, which we associate with reduced excitation of dark solitons and phonons.

Throughout the 3D Thomas-Fermi regime, the damping is found to be well described by a universal relation, which depends on the *dimensionless* defect strength V_D/μ and velocity v_0/c_0. The universal damping peaks at $v_0/c_0 \sim 1$ for any V_D/μ and scales as $(V_D/\mu)^2$ for all μ. As μ decreases, the peak damping rate decreases as well, consistent with the disappearance of the phonon portion of the excitation spectrum as $c_0 \to 0$. Damping in the quasi-1D regime is qualitatively different. In this case, we find, for fixed *absolute* V_D and v_0, that β is independent of μ. In this regime, damping is accompanied by fragmentation and spreading of the cloud, with the damping monotonically increasing with V_D/E_K, where E_K is the maximum single-particle kinetic energy.

A particularly intriguing possibility for the future is to explore the transport properties of a weakly attractive gas. In the case of a disordered potential, the opportunity to study the transport properties of bright matter-wave solitons [75] with the prospect to observe Anderson localization in such systems exists [76,77]. For a single defect, there is also a possibility for the creation of coherently split solitons or solitonic Schrödinger's cat states [78–80].

[1] M. H. Anderson, J. R. Ensher, M. R. Matthews, C. E. Wieman, and E. A. Cornell, Science **269**, 198 (1995).

[2] C. C. Bradley, C. A. Sackett, J. J. Tollett, and R. G. Hulet, Phys. Rev. Lett. **75**, 1687 (1995).

[3] K. B. Davis, M. O. Mewes, M. R. Andrews, N. J. van Druten, D. S. Durfee, D. M. Kurn, and W. Ketterle, Phys. Rev. Lett. **75**, 3969 (1995).

[4] I. Bloch, J. Dalibard, and W. Zwerger, Rev. Mod. Phys. **80**, 885 (2008).

[5] C. Raman, M. Köhl, R. Onofrio, D. S. Durfee, C. E. Kuklewicz, Z. Hadzibabic, and W. Ketterle, Phys. Rev. Lett. **83**, 2502 (1999).

[6] R. Onofrio, C. Raman, J. M. Vogels, J. R. Abo-Shaeer, A. P. Chikkatur, and W. Ketterle, Phys. Rev. Lett. **85**, 2228 (2000).

[7] C. Raman, R. Onofrio, J. M. Vogels, J. R. Abo-Shaeer, and W. Ketterle, J. Low Temp. Phys. **122**, 99 (2001).

[8] K. W. Madison, F. Chevy, W. Wohlleben, and J. Dalibard, Phys. Rev. Lett. **84**, 806 (2000).

[9] J. R. Abo-Shaeer, C. Raman, J. M. Vogels, and W. Ketterle, Science **292**, 476 (2001).

[10] P. C. Haljan, I. Coddington, P. Engels, and E. A. Cornell, Phys. Rev. Lett. **87**, 210403 (2001).

[11] E. Hodby, G. Hechenblaikner, S. A. Hopkins, O. M. Maragò, and C. J. Foot, Phys. Rev. Lett. **88**, 010405 (2001).

[12] L. Fallani, C. Fort, and M. Inguscio, Adv. At. Mol. Opt. Phys. **56**, 119 (2008).

[13] L. Sanchez-Palencia and M. Lewenstein, Nat. Phys. **6**, 87 (2010).

[14] D. Reppy, J. Low Temp. Phys. **87**, 205 (1992).

[15] J. Fortágh, H. Ott, S. Kraft, A. Günther, and C. Zimmermann, Phys. Rev. A **66**, 041604 (2002).

[16] A. E. Leanhardt, Y. Shin, A. P. Chikkatur, D. Kielpinski, W. Ketterle, and D. E. Pritchard, Phys. Rev. Lett. **90**, 100404 (2003).

[17] M. P. A. Jones, C. J. Vale, D. Sahagun, B. V. Hall, and E. A. Hinds, Phys. Rev. Lett. **91**, 080401 (2003).

[18] J. Estève, C. Aussibal, T. Schumm, C. Figl, D. Mailly, I. Bouchoule, C. I. Westbrook, and A. Aspect, Phys. Rev. A **70**, 043629 (2004).

[19] K. E. Strecker, G. B. Partridge, A. G. Truscott, and R. G. Hulet, Nature (London) **417**, 150 (2002).

[20] M. Junker, D. Dries, C. Welford, J. Hitchcock, Y. P. Chen, and R. G. Hulet, Phys. Rev. Lett. **101**, 060406 (2008).

[21] S. E. Pollack, D. Dries, M. Junker, Y. P. Chen, T. A. Corcovilos, and R. G. Hulet, Phys. Rev. Lett. **102**, 090402 (2009).

[22] J. Billy, V. Josse, Z. Zuo, A. Bernard, B. Hambrecht, P. Lugan, D. Clément, L. Sanchez-Palencia, P. Bouyer, and A. Aspect, Nature (London) **453**, 891 (2008).

[23] G. Roati, C. D'Errico, L. Fallani, M. Fattori, C. Fort, M. Zaccanti, G. Modugno, M. Modugno, and M. Inguscio, Nature (London) **453**, 895 (2008).

[24] L. Landau, J. Phys. (USSR) **5**, 51 (1941).

[25] D. R. Tilley and J. Tilley, *Superfluidity and Superconductivity* (IOP, London, 1990).

[26] C. J. Pethick and H. Smith, *Bose-Einstein Condensation in Dilute Gases* (Cambridge University Press, Cambridge, UK, 2002).

[27] E. Zaremba, Phys. Rev. A **57**, 518 (1998).

[28] G. M. Kavoulakis and C. J. Pethick, Phys. Rev. A **58**, 1563 (1998).

[29] S. Stringari, Phys. Rev. A **58**, 2385 (1998).

[30] L. Salasnich, A. Parola, and L. Reatto, Phys. Rev. A **65**, 043614 (2002).

[31] A. M. Kamchatnov and V. S. Shchesnovich, Phys. Rev. A **70**, 023604 (2004).

[32] P. O. Fedichev and G. V. Shlyapnikov, Phys. Rev. A **63**, 045601 (2001).

[33] T. Frisch, Y. Pomeau, and S. Rica, Phys. Rev. Lett. **69**, 1644 (1992).

[34] Y. P. Chen, J. Hitchcock, D. Dries, M. Junker, C. Welford, and R. G. Hulet, Phys. Rev. A **77**, 033632 (2008).

[35] S. E. Pollack, D. Dries, and R. G. Hulet, Science **326**, 1683 (2009).

[36] J. E. Lye, L. Fallani, M. Modugno, D. S. Wiersma, C. Fort, and M. Inguscio, Phys. Rev. Lett. **95**, 070401 (2005).

[37] D. Clément, A. F. Varón, M. Hugbart, J. A. Retter, P. Bouyer, L. Sanchez-Palencia, D. M. Gangardt, G. V. Shlyapnikov, and A. Aspect, Phys. Rev. Lett. **95**, 170409 (2005).

[38] T. Schulte, S. Drenkelforth, J. Kruse, W. Ertmer, J. Arlt, K. Sacha, J. Zakrzewski, and M. Lewenstein, Phys. Rev. Lett. **95**, 170411 (2005).

[39] J. W. Goodman, *Speckle Phenomena in Optics* (Roberts and Company, Greenwood Village, CO, 2007).

[40] S. G. Bhongale, P. Kakashvili, C. J. Bolech, and H. Pu, e-print arXiv:1003.2608.

[41] A. Radouani, Phys. Rev. A **68**, 043620 (2003).

[42] A. Radouani, Phys. Rev. A **70**, 013602 (2004).

[43] M. Modugno, Phys. Rev. A **73**, 013606 (2006).

[44] M. Albert, T. Paul, N. Pavloff, and P. Leboeuf, Phys. Rev. Lett. **100**, 250405 (2008).

[45] T. Schulte, S. Drenkelforth, G. K. Büning, W. Ertmer, J. Arlt, M. Lewenstein, and L. Santos, Phys. Rev. A **77**, 023610 (2008).

[46] S. Drenkelforth, G. K. Buning, J. Will, T. Schulte, N. Murray, W. Ertmer, L. Santos, and J. J. Arlt, New J. Phys. **10**, 045027 (2008).

[47] C. C. Bradley, C. A. Sackett, and R. G. Hulet, Phys. Rev. Lett. **78**, 985 (1997).

[48] R. Meppelink, S. B. Koller, J. M. Vogels, H. T. C. Stoof, and P. van der Straten, Phys. Rev. Lett. **103**, 265301 (2009).

[49] R. G. Scott and D. A. W. Hutchinson, Phys. Rev. A **78**, 063614 (2008).

[50] A. Görlitz *et al.*, Phys. Rev. Lett. **87**, 130402 (2001).

[51] F. Schreck, L. Khaykovich, K. L. Corwin, G. Ferrari, T. Bourdel, J. Cubizolles, and C. Salomon, Phys. Rev. Lett. **87**, 080403 (2001).

[52] A. M. Leszczyszyn, G. A. El, Y. G. Gladush, and A. M. Kamchatnov, Phys. Rev. A **79**, 063608 (2009).

[53] P. Leboeuf and N. Pavloff, Phys. Rev. A **64**, 033602 (2001).

[54] N. Pavloff, Phys. Rev. A **66**, 013610 (2002).

[55] G. Theocharis, P. Kevrekidis, H. Nistazakis, D. Frantzeskakis, and A. Bishop, Phys. Lett. A **337**, 441 (2005).

[56] R. Carretero-González, P. Kevrekidis, D. Frantzeskakis, B. Malomed, S. Nandi, and A. Bishop, Math. Comput. Simul. **74**, 361 (2007).

[57] S. Dettmer *et al.*, Phys. Rev. Lett. **87**, 160406 (2001).

[58] P. Engels and C. Atherton, Phys. Rev. Lett. **99**, 160405 (2007).

[59] V. Hakim, Phys. Rev. E **55**, 2835 (1997).

[60] M. Haddad and V. Hakim, Phys. Rev. Lett. **87**, 218901 (2001).

[61] C. K. Law, C. M. Chan, P. T. Leung, and M.-C. Chu, Phys. Rev. Lett. **85**, 1598 (2000).

[62] C. K. Law, C. M. Chan, P. T. Leung, and M. C. Chu, Phys. Rev. Lett. **87**, 218902 (2001).

[63] O. Lahav, A. Blumkin, C. Gordon, and J. Steinhauer, e-print arXiv:0906.1337.

[64] L. J. Garay, J. R. Anglin, J. I. Cirac, and P. Zoller, Phys. Rev. Lett. **85**, 4643 (2000).

[65] R. Balbinot, A. Fabbri, S. Fagnocchi, A. Recati, and I. Carusotto, Phys. Rev. A **78**, 021603 (2008).

[66] I. Carusotto, S. Fagnocchi, A. Recati, R. Balbinot, and A. Fabbri, New J. Phys. **10**, 103001 (2008).

[67] S. Burger, K. Bongs, S. Dettmer, W. Ertmer, K. Sengstock, A. Sanpera, G. V. Shlyapnikov, and M. Lewenstein, Phys. Rev. Lett. **83**, 5198 (1999).

[68] J. Denschlag *et al.*, Science **287**, 97 (2000).

[69] B. P. Anderson, P. C. Haljan, C. A. Regal, D. L. Feder, L. A. Collins, C. W. Clark, and E. A. Cornell, Phys. Rev. Lett. **86**, 2926 (2001).

[70] Z. Dutton, M. Budde, C. Slowe, and L. V. Hau, Science **293**, 663 (2001).

[71] A. Weller, J. P. Ronzheimer, C. Gross, J. Esteve, M. K. Oberthaler, D. J. Frantzeskakis, G. Theocharis, and P. G. Kevrekidis, Phys. Rev. Lett. **101**, 130401 (2008).

[72] J. J. Chang, P. Engels, and M. A. Hoefer, Phys. Rev. Lett. **101**, 170404 (2008).

[73] A. Muryshev, G. V. Shlyapnikov, W. Ertmer, K. Sengstock, and M. Lewenstein, Phys. Rev. Lett. **89**, 110401 (2002).

[74] T. Tsuzuki, J. Low Temp. Phys. **4**, 441 (1971).

[75] E. Akkermans, S. Ghosh, and Z. H. Musslimani, J. Phys. B **41**, 045302 (2008).

[76] Y. V. Kartashov and V. A. Vysloukh, Phys. Rev. E **72**, 026606 (2005).

[77] K. Sacha, C. A. Müller, D. Delande, and J. Zakrzewski, Phys. Rev. Lett. **103**, 210402 (2009).

[78] A. I. Streltsov, O. E. Alon, and L. S. Cederbaum, Phys. Rev. Lett. **100**, 130401 (2008).

[79] C. Weiss and Y. Castin, Phys. Rev. Lett. **102**, 010403 (2009).

[80] A. I. Streltsov, O. E. Alon, and L. S. Cederbaum, Phys. Rev. A **80**, 043616 (2009).